Controlling dominantly reactive (010) facets and impurity level by in-situ reduction of BiOIO₃ for enhancing photocatalytic activity

Jiang Wu[a,b,*], Kai Xu[a], Qizhen Liu[c], Zheng Ji[a], Chenhao Qu[a], XuemeiQi[a], Hui Zhang[a], Yu Guan[a], Ping He[a], Liangjun Zhu[a]

[a] College of Energy and Mechanical Engineering, Shanghai University of Electric Power, Shanghai 200090, China
[b] Shanghai Institute of Pollution Control and Ecological Security, Shanghai, China
[c] Shanghai Environment Monitoring Center, Shanghai 200030, China

ABSTRACT

In-situ reduction method was successfully taken out to control the highly reactive (010) facets and decline band gaps in interlining-I/BiOIO₃. It gave a fairly easy way to coordinate the control of bandgap engineering and structural engineering. The interlining-I provided an impurity level served as a plate for photo-generated electron to hop, which expanded the light reaction intensity and displayed excellent photocatalytic performance as well. The as-prepared samples were characterized and estimated for removing gas-phase Hg°. It demonstrated that there existed an optimization of I⁻ to construct a suitable impurity level for effectively separating and transferring electron-hole pairs. The corresponding structural engineering made the internal electric field(IEF) intensify, which was attributed to its increasing exposed surface in favor of obstructing their recombination in the bulk, generating a large number of essential species related to the larger exposed (010) facets to oxidize Hg° into Hg^{2+} under visible light. BI-1 showed the highest efficiency of 92.15%. However, because of the existence of light corrosion, a small part of the iodine ions may be oxidized to elemental iodine to volatilize, fortunately it could be regenerated to the original efficiency in the same preparation method. In addition, the samples with super photocatalytic properties and excellent electron transport properties also gave out a capacious prospect in CO_2 conversion, hydrogen evolution, NO removal, degradation of organic pollutants, also the super capacitors and batteries.

1. Introduction

Bismuth-based photocatalysts acquire worldwide attention for utilizing solar light to degrade pollutants [1–3], convert water to hydrogen, reduce carbon dioxide into organic fuels [4–8], and etc. And these are considered as the serious problems of consumption of non-renewable resources or the culprit in climate change human faces [9–11]. Among the photocatalysts, bismuth oxyiodate due to the low toxicity, peculiar crystal structures, has been a promising visible light-driven photocatalyst for excellent performance [12–14]. The non-centrosymmetric structures of aurivillius-type $(Bi_2O_2)^{2+}$ layers and $(IO_3)^-$ pyramids have the equivalent effect on electrons transportation [15]. More importantly, the internal electric field(IEF) plays a crucial role in separating photogenerated electron-hole pairs [16]. However, its applications are limited for relative larger bandgaps (about 3.0 eV) along with smaller absorbing boundary about 410 nm [14], and the higher recombination rates lead to the opposite consequence. Therefore, many researchers make efforts to modify bismuth oxyiodate, including fabricating heterojunctions [17–20], metal deposition [21–23] and doping [24–26].

In terms of doping, it can be divided into metal cation doping [27–29], non-metallic anion doping [30–32] and co-doping [33–35]. They all efficaciously provide a significant approach in bandgap engineering to produce an impurity level which can expand the absorption boundary and impede the recombination rates between photogenerated electrons and holes, and the impurity level serves as a springboard for photo-electronic transitions leading to higher photocatalytic activity. As the concentration of the doping increases, the space of charge region shortens, which leads in an intensive internal electric field. But more does not mean better, when doping concentration reaches certain amount, the space of charge region is more parochial than the penetration depth of light into the catalysts, so the width of the space-charge layers can be easily exceeded. Hence, it is notable to control the optimum.

From the above, we know that doping offers an impurity level in bandgap engineering to solve the problem of smaller light absorption boundary, but the high recombination rate still remains. However, only a few literatures [36,37] show that the structural engineering [38] plays a crucial role in strengthening the internal electric field and reducing the recombination rate of photogenerated carriers. Therefore, combining with structural engineering to solve the high recombination rate is particularly important.

Herein, in this work, we creatively used the doping method to co-ordinate the control of bandgap engineering and structural engineering for the first time. Specifically, we successfully manufactured the interlining-I/BiOIO$_3$ by in-situ reduction to incorporate iodine, which could not only narrow the band gap by providing decreasing impurity levels, but also control the dominantly reactive (010) facets leading to larger IEF, which effectively prevents recombination for excellent photocatalytic activity. It also supplied a meaningful application for removing gas-phase Hg° in the flue gas from coal combustion power station. The gas-phase Hg° with extreme volatility, persistence and bioaccumulation was rather hard to remove while the interlining-I/BiOIO$_3$ provided a perfect treatment. Beyond that it also gives out an extensive prospect in CO$_2$ conversion, hydrogen evolution, NO removal [39], degradation of organic pollutants [40,41], also the super capacitors and batteries due to the excellent electron transport properties and photocatalytic performance [10,25,42,43].

2. Experimental section

2.1. Preparation of modified BiOIO$_3$

The chemicals were all analytic grade reagents and without further purification. A one-step in-situ reduction method was used to prepare Iodine ion doped BiOIO$_3$. 4 mmol Bi(NO$_3$) ·5H$_2$O and 4 mmol KIO$_3$ were first dissolved into a mixed solution of 60 ml deionized water and 4 ml 67%(w/w) HNO$_3$. Then thiourea in different molar ratios of 0%, 0.5%, 1%, 2%, 4%, 8% relative to Bi(NO$_3$) ·5H$_2$O, which was reducible in acidic solution (Eq. (1)), were added into the above solution and stirred for 30 min. Afterwards the mixture was transferred into a 100 ml Teflon lined stainless autoclave and heated at 150 °C for 20 h. Finally, the products were washed with deionized water and anhydrous ethanol for three times respectively. The as-acquired samples with different molar ratios of thiourea were denoted as BI-0, BI-0.5, BI-1, BI-2, BI-4 and BI-8.

$$2SC(NH_2)_2 - 2e^- \rightleftarrows 2SCN_2H_3 + 2H^+ \tag{1}$$

2.2. Characterization

The crystal and phase structures were checked by X-ray diffraction (XRD, Bruker D8 Advance Diffractometer, Germany) with Cu Kα, which scanning range was 5–70° (scan rate 2° min^{-1}). For the further purpose of elemental composition, X-ray photoelectron spectroscopy (XPS) was carried out with Al Kα X-ray radiation which operating at 250 W (PHI5300, USA). The microstructure and morphology of the catalyst was detected using a scanning electron microscope (SEM, Phillips XL-30 FEG/NEW). The specific microstructure and shape was captured by transmission electron microscopy (TEM, Phillips Model CM200). High resolution TEM (HRTEM) was used to observe the crystal internal structure, atomic arrangement and a lot of fine structure. The energy-dispersive x-ray spectroscopy (EDS) was adopted to analyze the species and content of elements in the material micro-area. Brunauer-Emmett-Teller (BET) method (Micromeritics ASAP 2020) test the N$_2$ adsorption/desorption data for calculating the specific surface area and porosity. Fourier transform infrared (FTIR) was utilized to detect the local construction and the composition of the material related to the bonding states of the compounds with the range 4000–400 cm^{-1}. UV–vis diffuse reflectance spectra (UV–vis DRS) (SHIMADZU UV-3600, Japan) was used to obtain the optical absorption properties recorded over the range

290–700 nm. Barium sulfate (BaSO$_4$) was used as a reference standard. The photoluminescence (PL) spectra of the catalysts were performed on a fluorescence spectrophotometer. (HORIBA iHR550, America) with range of 200–800 nm and excited at 320 nm.

2.3. Photocatalytic activity test

The experiment system contained three main parts: (i) Simulated flue gas system; (ii) Photocatalytic reactor; (iii) Online mercury analyzer, which was similar to that in our previous works [44–46]. The gas cylinder was released with a flow rate of 1.2 L/ min of nitrogen, in the process of transmission, the N$_2$ flow was divided into two branches, one stream was 1 L/min, another was 0.2 L/min passing through the U-shape permeating tube heated at 50 °C in the water bath, in order to produce stable Hg° vapor to the system (55 μg/m^3). Mass flow meters (MFC, CS200 type) were utilized to command the flow rates. The photocatalytic activity test was implemented with 10 mg as-prepared catalyst applied to the quartz glass under the 9 W LED light with the filter (λ < 400 nm). The original Hg° concentration (55 μg/m^3) would decrease because of photocatalytic oxidation, which was measured by an online mercury analyzer (RA-915-M, Lumex Ltd., Russia) based on atomic absorption spectrometry. Hg° removal efficiency under LED irradiation condition was calculated according to the equation below.

$$\eta_{Hg^0}(\%) = (1 - Hg_{out}^0/Hg_{in}^0) \times 100\% \tag{2}$$

where Hg_{in}^0 represented Hg° concentration (μg/m^3) at the inlet of the system and Hg_{out}^0 represented the outlet. The final parts of the experimental reaction were activated carbon bottle and KMnO$_4$ absorption liquid for purifying the exhaust gas.

3. Results and discussion

3.1. Characterization of interlining-I/BiOIO$_3$

Fig. 1a shows the XRD patterns of as-prepared pure BiOIO$_3$ (BI-0) and different molar ratios of interlining-I/BiOIO$_3$ (BI-X, X = 0.5, 1, 2, 8). The diffraction peaks of BI-0 are completely suitable to Inorganic Crystal Structure Database ICSD # 262019 (space group: Pca21; a = 5.6584(4), b = 11.0386(8), c = 5.7476(4) Å) [15]. Different peaks corresponding to distinct indices of crystal face at specific 2θ values are listed in detail [47]. In addition to the intensity and width, no other impurity peaks have been inspected of the interlining-I/BiOIO$_3$. It confirms that in-situ reduction I ion does not form other substances, such as BiOI, but stays in the as-prepared sample. With the increasing of thiourea concentration, the intensity of (121) peak of interlining-I/BiOIO$_3$ increases gradually and then decreases, BI-1 reaches the maximum, suggesting that appropriate amount of in-situ reduction I ion improves the crystallinity, however too much doping can be counterproductive. Interestingly, a noteworthy part in the enlarged image Fig. 1b, (010) peak, which is assumed to be the exposed facet of all interlining-I/BiOIO$_3$, shows a slight red shift relative to BI-0, but in the former, (010) peak undertakes a gradual left-shift with increasing thiourea concentration, implying that interlining-I/BiOIO$_3$ own better photosensitivity, simultaneously in-situ reduction I ion is believed to dope into the lattice of BI-0 according to Bragg's Law (Eqs. (3)):

$$n\lambda = 2d\sin2\theta \tag{3}$$

d represents the interplanar spacing, θ is the angle between the incident X-ray and the corresponding crystal plane, λ is the wavelength of the X-ray, and n is the diffraction order. It's easy to understand that "2 θ" and "d" are inversely proportional, when 2 θ decreases, the lattice spacing enlarge because of in-situ reduction I ion insertion. In addition to the above, BI-1 may possess the highest exposure of (010) facet according to the widest and highest peak around 8 degrees [48]. However, what valence the iodine has been reduced to is still unknown, so another measure method, XPS analysis, is adopted to confirm the valence of
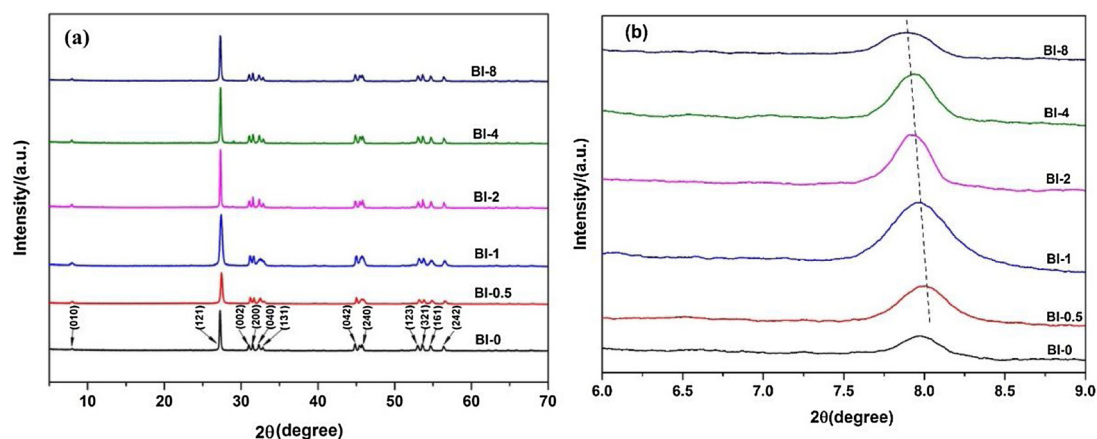
Fig. 1. XRD patterns of (a) as-prepared BI-0 and interlining-I/BiOIO$_3$ (b) enlarged image from 6°–9°.

interlining-I.

3.2. XPS measurements

The X-ray photoelectron spectroscopic (XPS) analysis is used to characterize the composition and oxidation state of corresponding elements in as-prepared samples. As shown in Fig. 2a, the whole spectrum verifies Bi, C, I, O in BI-0 and interlining-I/BiOIO$_3$, and Fig. 2b-d spread out the high-resolution spectra of the Bi 4f, I 3d, and O 1s. The weak peak of C 1s attributes to a carbon-containing

contamination from the apparatus [49]. In Fig. 2b two strong peaks of BI-1 with binding energies of 164.3 eV and 158.9 eV are assigned to Bi 4f$_{5/2}$ and Bi 4f$_{7/2}$ [50], a little left-shift related to BI-0, which corresponding energies are 164.1 eV and 158.8 eV, this might be due to the chemical environment change arising from in-situ reduction I ion insertion. Fig. 2c shows the high-resolution I 3d, the two strong peaks at 635.4 eV and 623.9 eV belong to I^{5+} 3d$_{3/2}$ and I^{5+} 3d$_{5/2}$ [25] respectively in BI-0, which is similar in BI-1, however there are two other brand new peaks existing with binding energy of 630.6 eV and 619.2 eV in BI-1, which are assigned to I^{3+} 3d$_{3/2}$ and I^{3+} 3d$_{5/2}$. The result
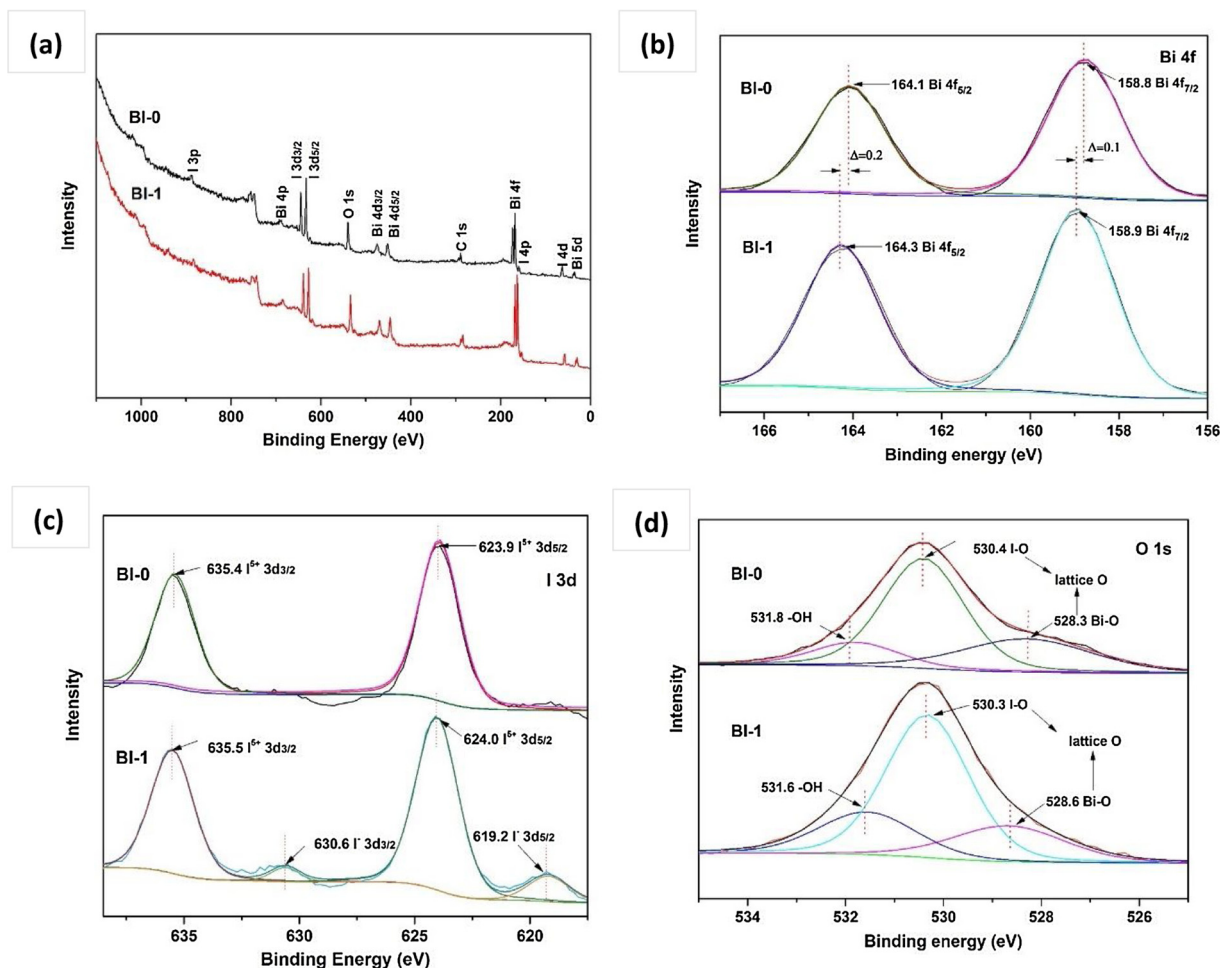

Fig. 2. Fully survey scanned XPS spectra of (a) BI-0 and BI-1;(b) high resolution XPS spectra of BI-0 and BI-1 for (b) Bi 4f, (c) I 3d, (d) O1s.

Table 1
XPS data of oxygen species of BI-0 and BI-1.

Sample name	BI-0	BI-1
Ads. %	12.7	20.7

confirms the valence of interling-I is −1, simultaneously linking to the XRD analysis, the in-situ reduction I ion from I^{+5} to I^{-} is successfully doped into the lattice. Last but not least, it is noteworthy to observe the change of O1 s shown as Fig. 2d. Three kinds of oxygen species in the as-prepared catalysts, i.e., surface hydroxyl groups [51], and lattice oxygen including I−O and BI−O. Here lists the XPS data of oxygen species in Table 1.

Ads. %: the percentage of the surface hydroxyl groups to total oxygen.

As can be seen, the ads. % of BI-1 is obviously higher than that of BI-0, assuming that larger specific surface area may adsorb more molecular H_2O in BI-1 due to inserting in-situ reduction I ion which enlarges the lattice spacing. In order to further study the surface of the bonds affected by the interling-I, the FT-IR spectra is adopted.

3.3. FT-IR spectroscopy

Fig. 3 shows the bond characteristics of functional groups of BI-0 and interling-I/BiOIO$_3$ detected by FT-IR spectra. The peak observed at 515.4 cm^{-1} is assigned to the vibration of BI−O band [26]. In the vicinity of BI−O is two strong peaks at 687.5 cm^{-1} and 763.7 cm^{-1} apiece corresponding to I−O stretching vibration [52]. While the rest two acuity peaks at a location of 1652.6 cm^{-1} and 3444.2 cm^{-1} are indexed to H−O−H and O−H for surface hydroxyl groups or adsorbed molecular H_2O [19]. The results better match the above XPS measurements, which define the elements of Bi, I, O and homologous bond of functional groups BI−O, I−O in lattice oxygen. Moreover, with in-situ reduction I ion incorporation, more bonds of H−O−H and O−H are produced attached to the surface, ultimately playing a leading role in photocatalytic activity. Furthermore, the superficial hydroxyl group and water assimilate photogenerated holes to create hydroxyl radicals, which possess super oxidation for removal of pollutants, withal impeding electron-hole recombination for optimizing photocatalysis. However how is bond groups-dependent surface structure?
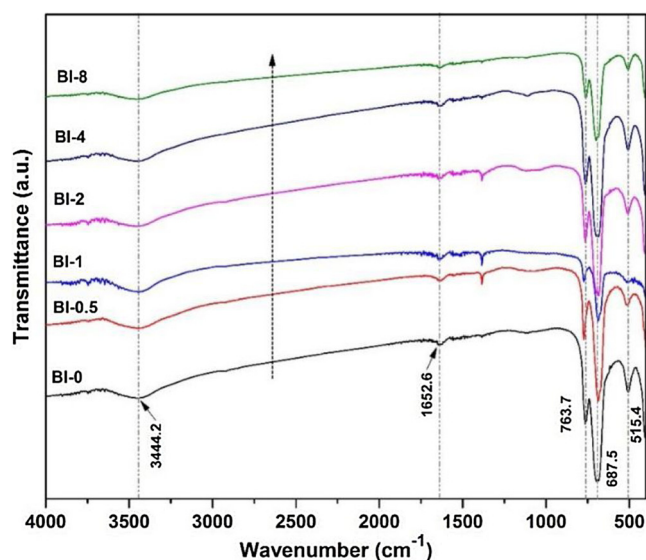

Fig. 3. The FTIR spectra of BI-0 and interling-I/BiOIO$_3$.

3.4. Morphology and structure analysis

3.4.1. SEM analysis
Fig. S1(a–d) shows the scanning electron microscope (SEM) images of BI-0 and interling-I/BiOIO$_3$ to reveal the surface structure and morphological characteristics. Compared with BI-0, the most typical distinction in BI-1 is incorporating iodine ion, BI-0 has nonuniform thick slabs with highly polished surfaces and neat cut edges, with length and width of several hundred nanometers, also thickness of about 50 nm. Differently BI-1 has the largest laminar layer of all, leading to high specific surface area. From Fig. S1(b–d), the laminar layers gradually break into smaller nanosheets with less angular, and ultimately turn into well-proportioned elliptical shape with average diameter of 150 nm, simultaneously occurring the reunion. It speculates that moderate interling-I pulls the lattice wide leading to the greater exposure of active crystal face (010), which is perpendicular to lattice fringe shown in the mechanism diagram Fig. 4h–k. Furthermore, the TEM and HRTEM analysis will make a proof.

3.4.2. TEM and HRTEM analysis
TEM images shown in Fig. 4a, c and e verify the results from SEM that the samples experience the process of crystal fragmentation and reunion as iodide ion concentration increases. In addition, the thickness is determined to be 17.78 nm. Fig. 4b and d shows the HRTEM images of BI-0 and BI-1 respectively, and the lattice distance is enlarged from 0.288 nm to 0.292 nm consistent with (002) facet. On the one hand, from mechanism diagram Fig. 4h–k, it can be seen that along the TEM perspective, that is, the y-axis, the distance of (001) facet is easier to detected than (100) facet, and it may explain why we cannot find (100) facet and the (010) facet, which is perpendicular to (001), and (100) facet is determined to be the exposed surface along with x–z axis. On the other hand, it is further testified that iodide ions are doped into the crystal lattice, and the widened (001) facet also enlarges the (010) facet shown in Fig. 4b and d, leading to the highest efficiency in removing Hg°. It indicates that the (010) facet is not just the main exposed surface in BiOIO$_3$, also the highly active exposed surface, which is in accordance with the next photocatalytic performance and the reported result [37,48,53].

The EDS and elemental mapping are shown in Fig. 4f and g. The results well define the atomic percentages and spatial distribution information for BI-1. The residual substances remaining in the reductant are effectively removed by centrifuging, and elements of Bi and I are uniformly distributed in all samples leading to homogenous microstructure and thermal stability.

3.4.3. Surface area analysis
The specific surface area (S_{BET}) is shown in Fig. 5, in which N_2 adsorption-desorption isotherms exhibit typical type IV with an H3 hysteresis loop, and all data are calculated in Table 2. S_{BET} of BiOIO$_3$ reveals the rule of gradual increase and then decrease along with the incremental iodine, and BI-1 has the highest value of all. It well affirms the SEM and TEM results above, the nonuniform thick slabs gradually become larger and thinner along with the increase of highly active exposed surfaces, then fracture and overlap.

3.5. Band gap control for optical properties

Fig. 6b show the optical properties of BI-0 and interling-I/BiOIO$_3$ by UV–vis DRS in ambient temperature. The absorption boundary of BI-0 is approximately 414 nm coinciding with many completed documents [22,26]. The optical absorption is enhanced along with gradual red shift from 414 nm to 442 nm of the absorption edge. To confirm the optical band gap energy of the samples, they are calculated based on the absorption spectrum according to the Eqs. (4) and (5) below [54,55].
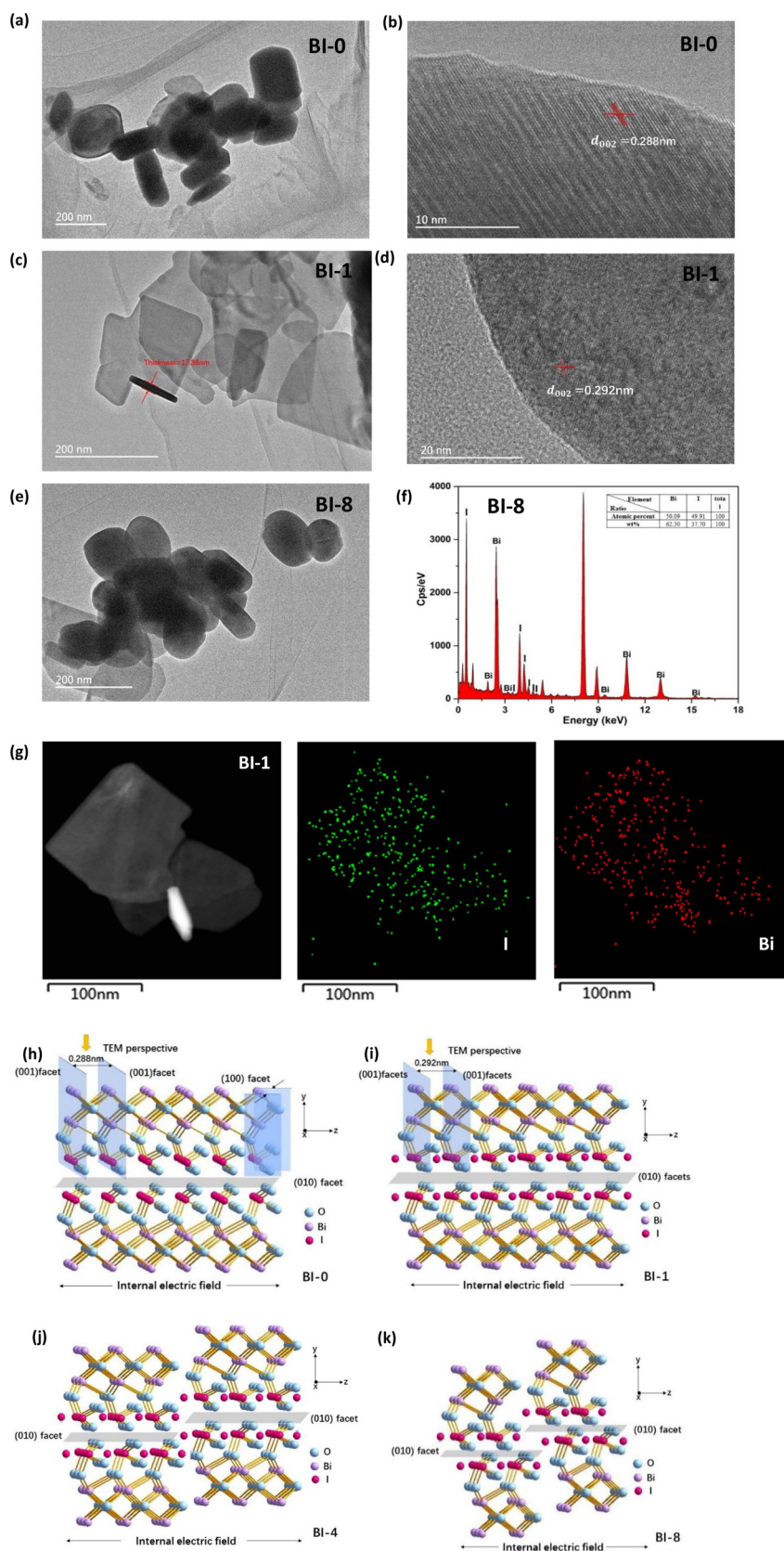
Fig. 4. TEM images of (a) BI-0, (c) BI-1, (e) BI-8; HRTEM images of (b) BI-0, (d)BI-1; (f) EDS images of BI-8; (g) Elemental mapping of BI-1; Mechanism diagram of active facets for (h) BI-0, (i) BI-1, (j) BI-4, (k) BI-8.
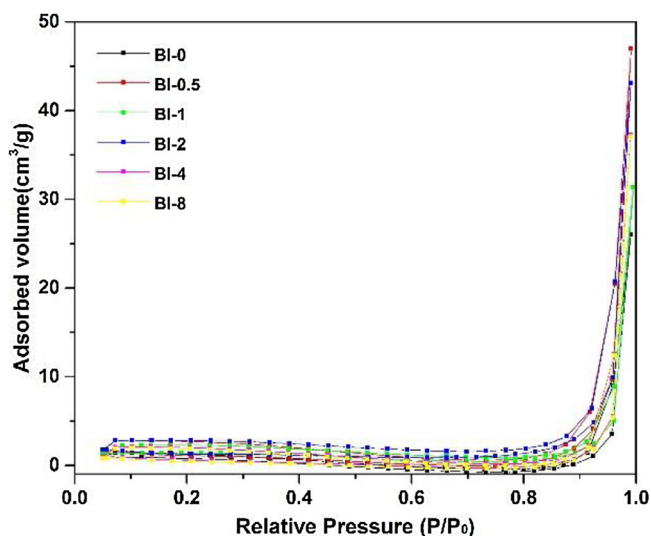
Fig. 5. N_2 adsorption-desorption isotherms of BI-0 and interlining-I/BiOIO$_3$.

$$Eg = 1240/\lambda_{Absorp.\,Edge} \tag{4}$$

$$\alpha h\nu = A(h\nu - Eg)^{n/2} \tag{5}$$

where α, $h\nu$, A, and Eg respectively represent the absorption coefficient, photonic energy, a constant and band gap. The n value is 4 which depends on the characteristics of indirect optical transition in BiOIO$_3$. Therefore, the Eg value can be determined from a plot of $(\alpha h\nu)^{1/2}$ versus $h\nu$ by extending the tangent line, the interception with x axis would be the value of the band gap. The Eg values are depicted in Table 2 and Fig. 6c which are found to be 2.99, 2.98, 2.93, 2.91, 2.86, and 2.80 eV for BI-X (X = 0, 0.5, 1, 2, 4, 8). Compared with pure BiOIO$_3$ (BI-0), the band gaps of interlining-I/BiOIO$_3$ narrow to a certain degree, which indicates that the doping of in-situ reduction I ion weakens the bandgap of BiOIO$_3$ and possibly provides an impurity level below the conduction band [24], thereby making interlining-I/BiOIO$_3$ more photosensitive. Furthermore, the band edge positions of BI-0 can be ascertained with the concept of electronegativity. The conduction band (CB) composed of Bi 6p, O 2p and I 5p orbitals and valence band (VB) potentials composed of O 2p orbitals can be calculated by the next Eqs. (6) and (7):
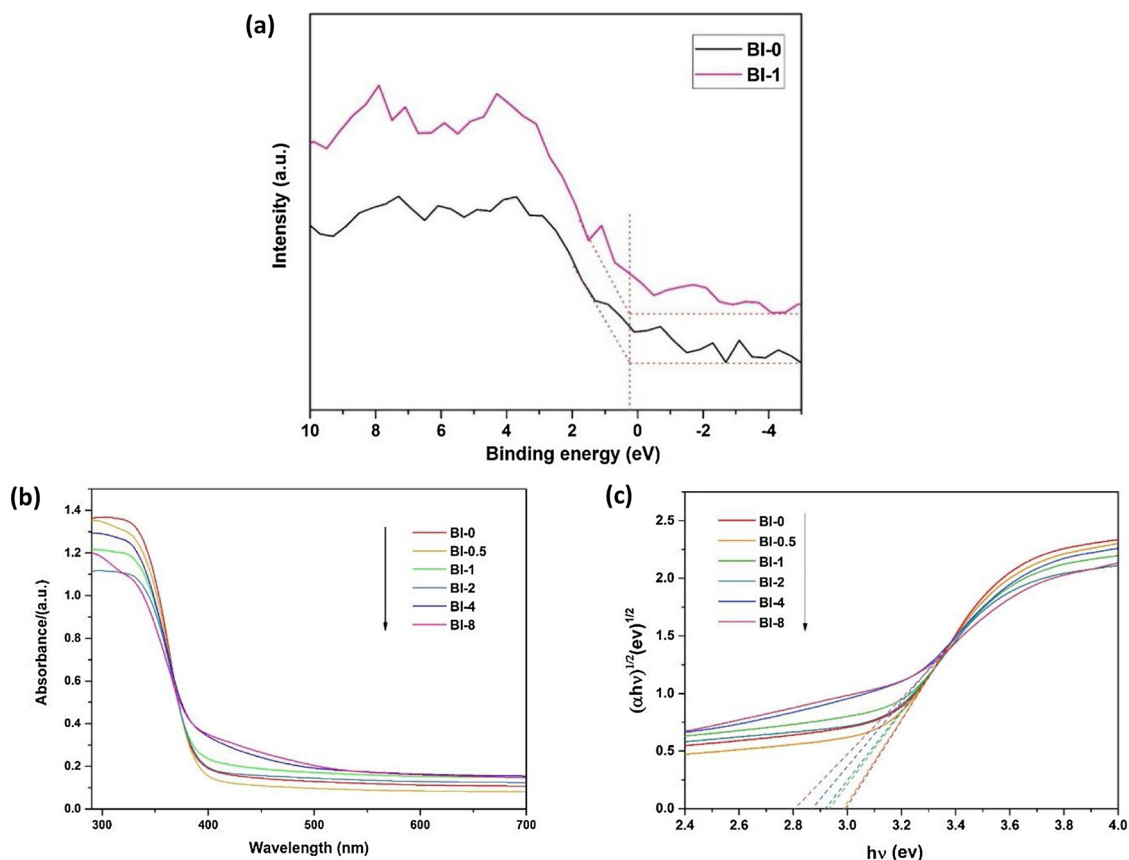
Table 2
The chemical and physical photocatalytic efficiency of BI-0 and interlining-I/BiOIO$_3$.

Samples	BET surface area (m^2/g)	Interstitial impurity potentials (eV)	Absorbing boundary (nm)	Bandgap (eV)	Hg° removal efficiency η(%)
BI-0	1.55	1.05	414	2.99	71.49
BI-0.5	2.72	1.06	416	2.98	79.04
BI-1	3.86	1.11	423	2.93	92.15
BI-2	3.44	1.13	426	2.91	71.74
BI-4	1.18	1.18	433	2.86	53.87
BI-8	1.09	1.24	442	2.80	50.97

Fig. 6. (a) VB XPS of BI-0 and BI-1; (b) UV–vis DRS spectra of BI-0 and interlining-I/BiOIO$_3$; (c) Band gap values of BI-0 and interlining-I/BiOIO$_3$.
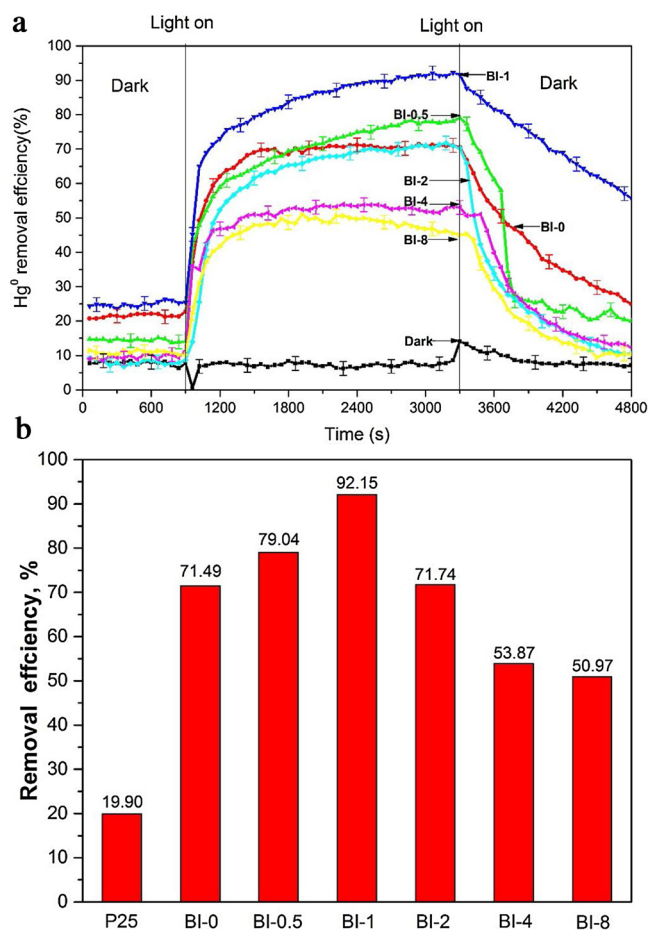
Fig. 7. (a) Mercury removal efficiency of all samples under visible light. (b) Comparison diagram of P25, pure BiOIO$_3$ and all interlining-I/BiOIO$_3$.

$$E_{VB} = \chi - E^e + 0.5E_g \tag{6}$$

$$E_{CB} = E_{VB} - E_g \tag{7}$$

where χ (ca. 7.04 eV for BiOIO$_3$) represents the electronegativity of the semiconductor expressed as the geometric mean of the electronegativity of the constituent atoms, E^e (ca. 4.5 eV) is the energy of free electrons on the hydrogen scale. The VB and CB potentials are 4.04 and 1.05 eV for BiOIO$_3$ respectively. In order to investigate the evolution of band structure for interlining-I/BiOIO$_3$, the valence band (VB XPS) Fig. 6a is exhibited. It's obvious to see that there is no shift in binding energy because the doped I does not transform the valence band position but gradually dropping the interstitial impurity potentials. The data of VB, CB and interstitial impurity potentials are shown in Table 2.

3.6. Photocatalytic performance

3.6.1. Hg° removal on the samples under LED irradiation

Hg° removal performances are examined under visible light irradiation, 9 W LED with filter($\lambda < 400$ nm), each experience is divided into three segments including 15 min in dark for adsorption-desorption equilibrium, 40 min in visible light irradiation for photocatalytic oxidation of mercury, and the rest 25 min in dark for the sake of revivification. As shown in Fig. 7a below, the blank experiment is tested to invest the adsorption (about 7 μg/m^3) of the whole system in that we can calculate the adsorption of the sample excluding the system's effect. In the moment of turning on the light the concentration is a little bit higher than in dark attributed to higher energy leading to higher concentration instantly, analogously to explain the phenomenon of depression when light off. In the case of BI-X, the mercury removal
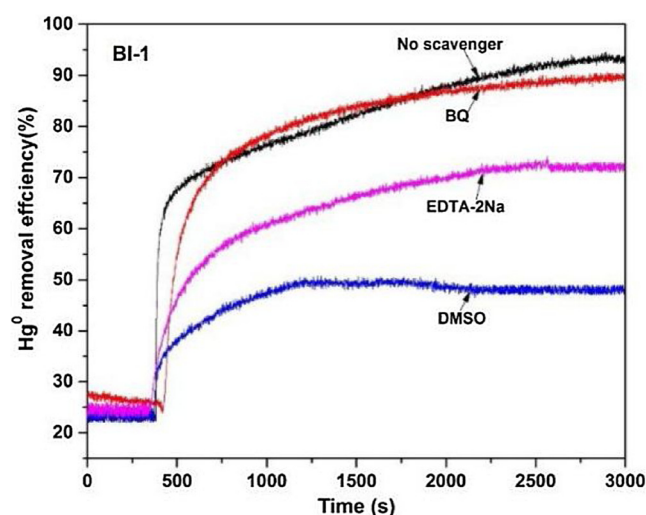

Fig. 8. Mercury removal efficiency with different scavengers under visible light.

efficiencies are 70.89%, 79.04%, 92.15%, 71.74%, 53.87%, and 50.96% which are shown in Table 1. Compared to both the P25 and the pure BiOIO$_3$ shown in Fig. 7b, the efficiency of interlining-I/BiOIO$_3$ is much higher than P25, it increases gradually and then decays regularly, while BI-1 exhibits the most excellent photocatalytic oxidation efficiency. That is to say, the concentration of doping iodine has an optimal value. It is also concluded from SEM and TEM, the suitable modifying iodine changes the morphology into glossy and large layer. Therefore, more (010) facets of the crystals are exposed leading to higher efficiencies. However excessive dopants firstly break the large layers into the small and then aggregate, leading to the less active exposure shown in Fig. 4h–k Besides, in terms of optical properties, the bandgaps are continuously and precisely controlled by incorporating the concentration of iodine, therefore, the samples can adsorb more light energy to enhance the catalytic activity.

3.6.2. Active species trapping measurements

In order to investigate the reaction process in the removal of Hg°, the trapping measurements are carried out to research the principal active species. There are three different quenchers benzoquinone (BQ), ethylene diaminetetraacetic acid disodium (EDTA-2Na), and dimethyl sulfoxide(DMSO)adding in BI-1 for capturing the superoxide radicals (·O$_2^-$), holes (h$^+$) and hydroxyl radicals (·OH) respectively. From Fig. 8, the mercury removal efficiency for BI-1 is almost the same as the first experience. The conduction band position of BI-1 is counted to be 1.11 eV in this work, which is lower than O$_2$/·O$_2^-$ (−0.28 eV) couple [56], so the cumulative electrons in CB of BI-1 have no ability to reduce O$_2$ into ·O$_2^-$. It is also concluded from the following experiment, there is not too much difference when adding BQ, hence ·O$_2^-$ does not yield and proves ineffective, this consequence is verified in our previous paper as well [15]. However, EDTA-2Na and DMSO have the efficiencies of about 70% and 50%, the removal efficiency of Hg° was inhibited significantly by h$^+$ and ·OH. In general, it is concluded that ·OH is the most essential factors in the process, and h$^+$ does subsequently.

3.6.3. Stability and regeneration of the catalysts

Cyclic stability and regeneration are important portions of the photocatalysts for practical application. Six cyclic tests are implemented to detect the stability in parallel surroundings shown in Fig. 9a. The photocatalytic activity shows only 10% decrease in the efficiency after six cycles, it is considered to own better stability and also have high photocatalytic efficiency about 80%. It assumes that the reduction of 10% results from the slight photochemical corrosion of iodide in the samples. The structures of the BI-1 before and after six
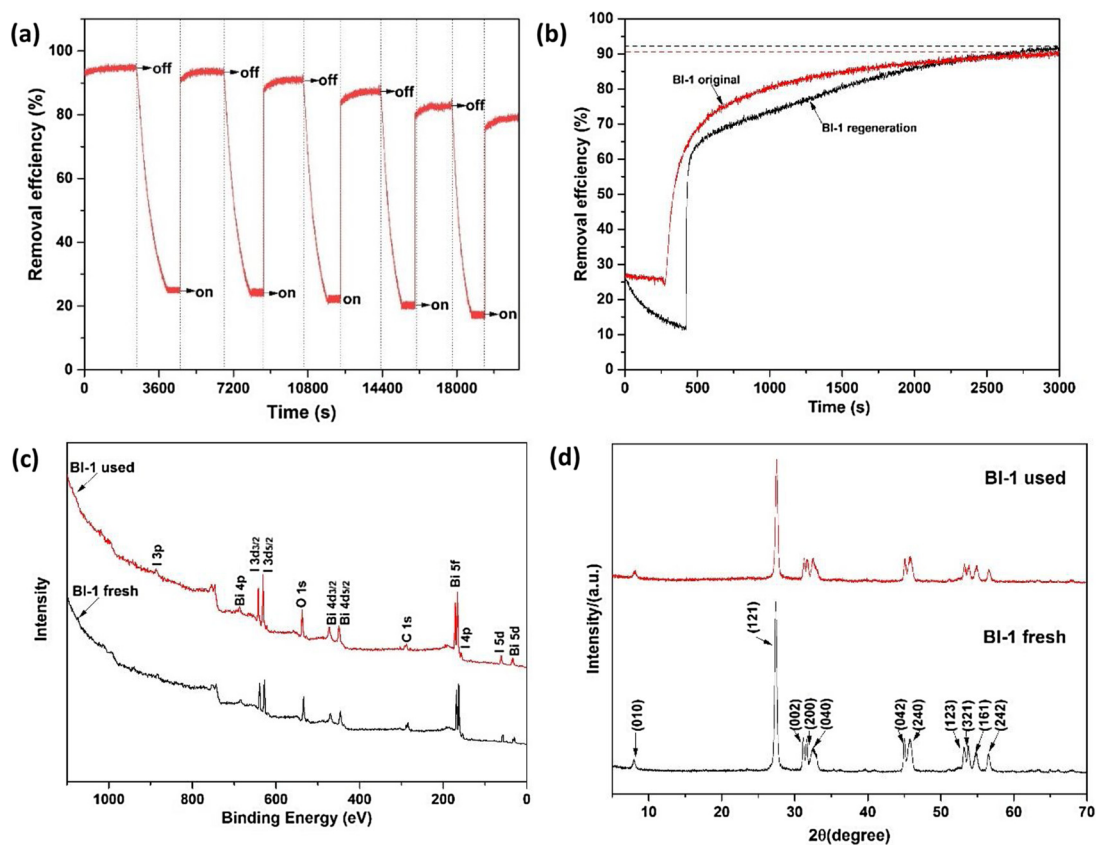
Fig. 9. (a) Cycle efficiency image of BI-1; (b) Regeneration image of BI-1; (c) Fully survey scanned XPS spectra of fresh and used BI-1; (d) XRD patterns of fresh and used BI-1.
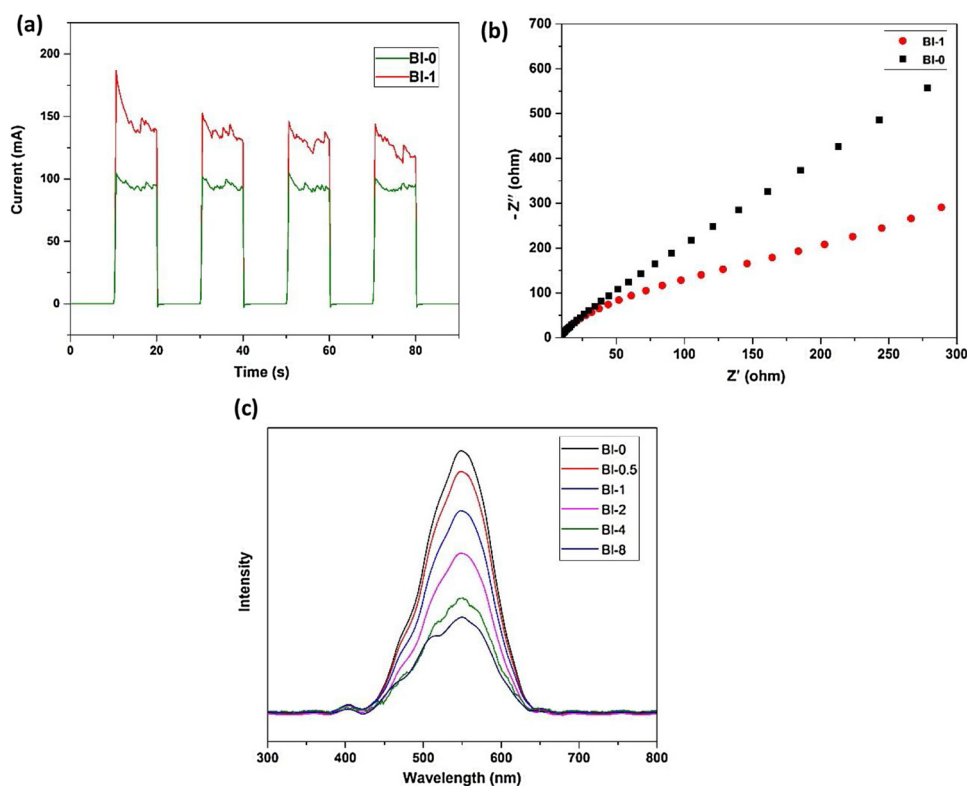

Fig. 10. (a) Transient photocurrent densities of BI-0 and BI-1; (b) EIS Nyquist plot of BI-0 and BI-1; (c) Photoluminescence emission spectra of all samples.
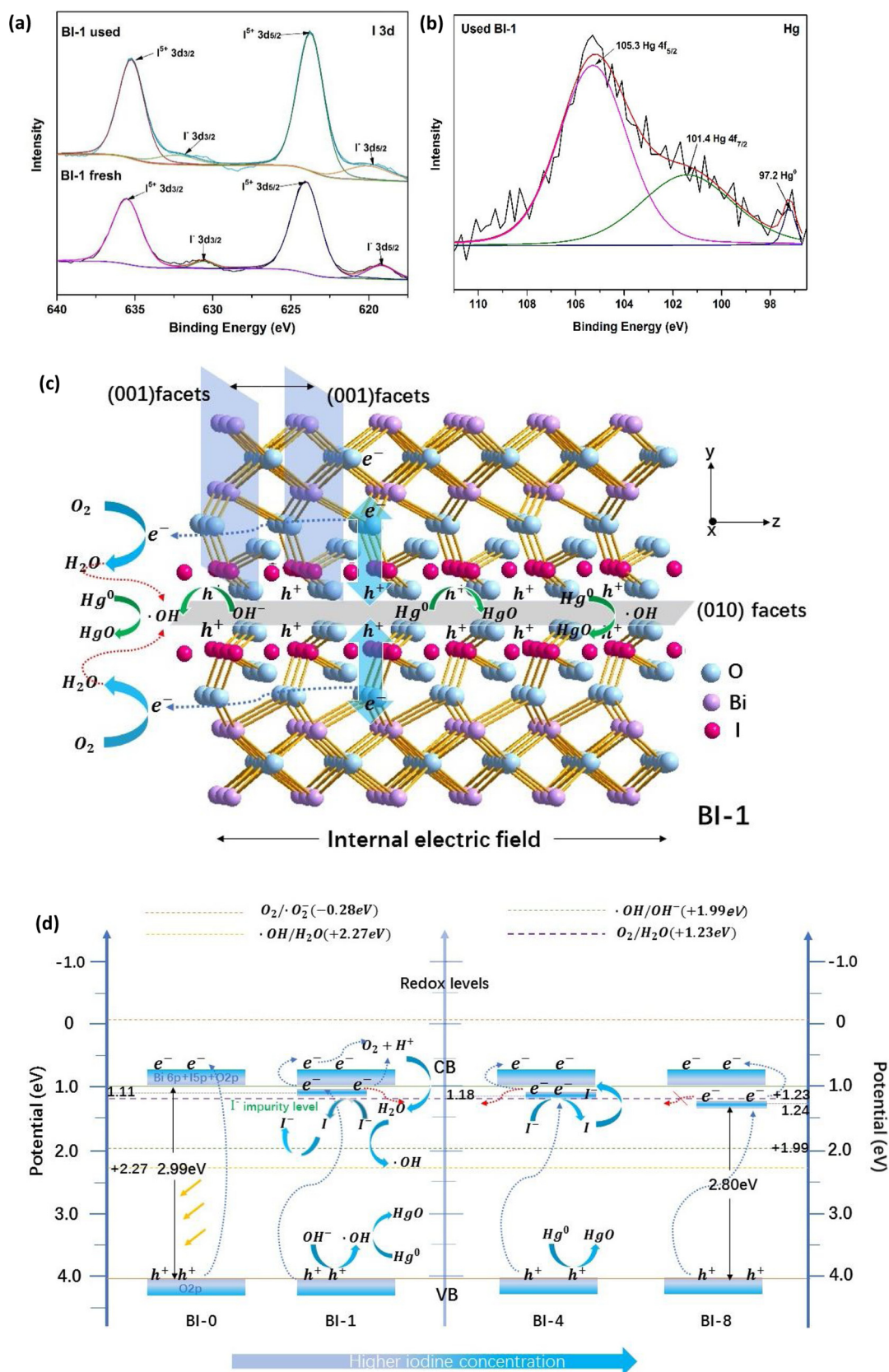
Fig. 11. High resolution XPS spectra of fresh and used BI-1 for (a) I 3d, (b) Hg; Photocatalytic mechanism diagrams of (c) highly active (010) facets for BI-1, (d) impurity levels for BI-0, BI-1, BI-4, BI-8.

consecutive cycles are characterized by the XPS and XRD analysis shown in Fig. 9c-d, fortunately there is no obvious distinctions in both patterns before and after the photocatalytic oxidation of Hg°. In summary, we put forward the concept of regeneration for BI-1, as exhibited in Fig. 9b. The used samples (after 6cycles) are utilized in same one-step in-situ reduction method to generate iodine which is consumed, simultaneously recovering the ability of photocatalytic oxidation of Hg°.

3.7. Mechanism analysis

3.7.1. Charge separation, transfer and recombination mechanism (STRM)

Photocurrent (PC), electrochemical impedance spectra (EIS) and photoluminescence (PL) measurements shown in Fig. 11a–c are conducted to research the photoelectron dynamics of charge separation, transfer and recombination respectively during the process [57].

The photocurrent responses of BI-0 and BI-1 are operated after four on-off cycles of visible light irradiation, the result is exhibited in Fig. 10a. When turning on the light, both photocurrents upraise instantly. BI-1 shows larger photocurrent density about 1.5 times than BI-0. The amplitudes of both samples are corresponding to the photocatalytic activity in removing Hg°. BI-1 owns better ability than BI-0 to separate the electron-hole pairs, which playing the leading role in reaction process.

EIS Nyquist plots are used to investigate the interface charge transfer process shown in Fig. 10b. It is obvious that the arc radius of BI-1 is smaller than BI-0, hence, the former cannot only easily separate electron-hole pairs, but also smoothly transfer them to the reactant interface for better reaction in that confronting less impedance. Moreover, the lifetime of electron-hole pairs can be calculated from Eqs. (8):

$$\tau = 1/2\pi f \tag{8}$$

Where f means the inverse minimum frequency. The lifetime of BI-1 is estimated to be 60.96 μs which is 1.211 times larger than BI-0 for 50.33 μs. That is to say BI-1 prolongs the existence of electron-hole pairs and thus allows more time to react. The low fluorescence intensity which is excited by 320 nm ultraviolet light in photoluminescence spectroscopy means the low recombination rate of photoexcited electron-hole pairs, oppositely represents high photocatalytic performance. As shown in Fig. 10c, the recombination of electron-hole pairs are effectively hindered by interlining-I concentration. The intensity descends gradually when existing more and more iodine, it is speculated that the higher impurity level position may take electron-hole pairs more time for recombination attributed to internal static electric field [58]. However, the low recombination rate is not the only decisive factor in the photocatalytic reaction, it is necessary to fully consider above three reasons that affect the separation, transfer and recombination of hole-electron pairs. On the one hand, it explains why the recombination rate of BI-1 is higher than that of BI-8, but it shows higher reaction efficiency. From another perspective, there is an optimum amount of iodine doping during the reaction.
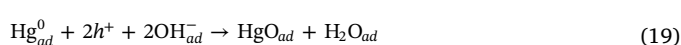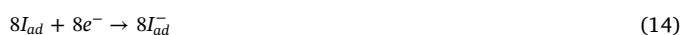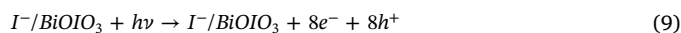
3.7.2. Photocatalytic reaction mechanism

In order to probe the reaction mechanism of interlining-I/BiOIO₃, the change before and after the reaction of BI-1 in XPS analysis is taken out for comparison as the best mercury removal efficiency sample. From Fig. 11a, the peak at around 630 eV indexed to I^- $3d_{3/2}$ has obvious shift, even fades away after the reaction. The phenomenon manifests that in-situ reduction I^- play an important role, because increasing I^- furnish a gradually decreasing impurity level versus to CB which contract the band gap for more extension of the visible light. But there exists some slight inactivation during a long time, in spite, I^- plays the media role of providing and receiving electronic. Besides, in term of high- resolution spectra of Hg emerged in Fig. 11b, there are three peaks at 105.3 eV, 101.4 eV, and 97.2 eV according to Hg $4f_{5/2}$, Hg $4f_{7/2}$ of HgO and Hg°(g) which is relatively few separately [59]. It comes to a conclusion that HgO is formed during the reaction, however

because of its low content, we hypothesize that BI-1 cannot well adsorb the HgO on its surface and is blown into the system through the gas flow due to a smaller specific surface area.

Combined with mechanism diagrams Fig. 11c and d, larger highly active exposed surfaces accompanying with intensifying internal electric field (IEF) and appropriate impurity level position contribute to effective separation of photogenerated electrons(e⁻) and holes(h⁺), also IEF along the z-axis prompts electrons to transfer to (001) facets [37], and holes to transfer to (010) facets. The transfer of electrons and holes in a vertical direction to different planes further reflects the effective separation. The cumulative electrons of CB in (001) facets cannot reduce O_2 to $\cdot O_2^-$ because of the potential of the electrons (+1.05 eV) is higher than $O_2/\cdot O_2^-$ (−0.28 eV) couple, however the electrons are consumed to generate H_2O combined with O_2 (O_2/H_2O + 1.23 eV). The generated H_2O are effectively oxidized to $\cdot OH$ ($\cdot OH/H_2O$ + 2.27 eV) through h⁺ of VB(+ 4.04 eV) in (010) facets. Beyond that the main active species $\cdot OH$ can also be produced directly through oxidizing OH^- ($\cdot OH/OH^-$ + 1.99 eV) by holes. To sum up, in BI-1, larger active exposed surfaces (010) facets can attract holes to generate more hydroxyl radicals which are the most essential factors involving in the reaction, leading to the highest efficiency in photocatalytic performance.

At last the existing holes and produced $\cdot OH$ can easily oxidize Hg° into HgO. The reaction process can be described as the following Eqs. (9)–(19). It well interprets that although there is a small amount of H_2O in the samples and system, however it acts as a medium without being consumed in reactive circulation. Moreover, it is noteworthy in BI-8 that the electrons cannot reduce O_2 to H_2O because of the negative potential with respect to O_2/H_2O (+1.23 eV) couple, lessening the origin of part of the $\cdot OH$, which explains why BI-8 has low efficiency.

$$I^-/BiOIO_3 + h\nu \rightarrow I^-/BiOIO_3 + 8e^- + 8h^+ \tag{9}$$

$$4H_2O_{ad} \rightarrow 4H^+ + 4OH^-_{ad} \tag{10}$$

$$8I^-_{ad} \rightarrow 8I_{ad} + 8e^- \tag{11}$$

$$2O_2 + 8H^+ + 8e^- \rightarrow 4H_2O \tag{12}$$

$$4H_2O + 4h^+ \rightarrow 4\cdot OH + 4H^+ \tag{13}$$

$$8I_{ad} + 8e^- \rightarrow 8I^-_{ad} \tag{14}$$

$$2OH^-_{ad} + 2h^+ \rightarrow 2\cdot OH_{ad} \tag{15}$$

$$2Hg^0(g) + surface \rightarrow 2Hg^0_{ad} \tag{16}$$

$$2Hg^0(g) + 4\cdot OH \rightarrow 2HgO + 2H_2O_{ad} \tag{17}$$

$$Hg^0_{ad} + 2\cdot OH_{ad} \rightarrow HgO + H_2O_{ad} \tag{18}$$

$$Hg^0_{ad} + 2h^+ + 2OH^-_{ad} \rightarrow HgO_{ad} + H_2O_{ad} \tag{19}$$

4. Conclusions

In-situ reduction method was successfully taken out to control the dominantly reactive (010) facets and decline band gaps in interlining-I/BiOIO₃. There existed an optimization of BI-1, and the highest mercury removal efficiency even reached 92.15% under the visible light. During the reaction, $\cdot OH$ was generated in (010) facets, which played a vital role in oxidizing gas-phase Hg°. I^- in the samples confronted a little loss after a long reaction, but it could be restored through regenerating. All of the discoveries provide a vast application prospect in many fields for photocatalytic oxidation of pollutants, CO_2 conversion, hydrogen evolution, NO removal, degradation of organic pollutants, also the super capacitor and battery due to the excellent electron transport properties.

Acknowledgments

Appendix A. Supplementary data

Supplementary material related to this article can be found, in the online version, at doi:https://doi.org/10.1016/j.apcatb.2018.03.046.

References

[1] L. Ye, X. Jin, X. Ji, C. Liu, Y. Su, H. Xie, C. Liu, Chem. Eng. J. 291 (2016) 39–46.
[2] J. Liu, J. Meeprasert, S. Namuangruk, K. Zha, H. Li, L. Huang, P. Maitarad, L. Shi, D. Zhang, J. Phys. Chem. C 121 (2017) 4970–4979.
[3] L. Huang, K. Zha, S. Namuangruk, A. Junkaew, X. Zhao, H. Li, L. Shi, D. Zhang, Catal. Sci. Technol. 6 (2016) 8516–8524.
[4] Y. Ma, X. Wang, Y. Jia, X. Chen, H. Han, C. Li, Chem. Rev. 114 (2014) 9987–10043.
[5] S. Rahimnejad, J.H. He, F. Pan, X.E. Lee, W. Chen, K. Wu, G.Q. Xu, Mater. Res. Express 1 (2014) 045044.
[6] Y.P. Yuan, L.W. Ruan, J. Barber, S.C.J. Loo, C. Xue, Energy Environ. Sci. 7 (2014) 3934–3951.
[7] H. Huang, X. Li, J. Wang, F. Dong, P.K. Chu, T. Zhang, Y. Zhang, ACS Catal. 5 (2015) 150603114219008.
[8] L. Shang, T. Bian, B. Zhang, D. Zhang, L.Z. Wu, C.H. Tung, Y. Yin, T. Zhang, Angew. Chem. 53 (2014) 250.
[9] G.J. Choi, Q. Zhu, D.C. Miller, C.J. Gu, R.R. Knowles, Nature 539 (2016) 268.
[10] K. Maeda, K. Teramura, D. Lu, T. Takata, N. Saito, Y. Inoue, K. Domen, Nature 440 (2006) 295.
[11] J.D. Cuthbertson, D.W.C. Macmillan, Nature 519 (2015) 74.
[12] H. Zhao, F. Tian, R. Wang, R. Chen, Rev. Adv. Sci. Eng. 3 (2014) 3–27.
[13] J. Li, Y. Yu, L. Zhang, Nanoscale 6 (2014) 8473.
[14] X. Sun, J. Wu, Q. Li, Q. Liu, Y. Qi, L. You, Z. Ji, P. He, P. Sheng, J. Ren, Appl. Catal. B: Environ. 218 (2017) 80–90.
[15] J. Wu, X. Chen, C. Li, Y. Qi, X. Qi, J. Ren, B. Yuan, B. Ni, R. Zhou, J. Zhang, Chem. Eng. J. 304 (2016) 533–543.
[16] L. Li, P.A. Salvador, G.S. Rohrer, Nanoscale 6 (2014) 24.
[17] F. Dong, T. Xiong, Y. Sun, Y. Zhang, Y. Zhou, Chem. Commun. 51 (2015) 8249–8252.
[18] H. Zhang, C.G. Niu, S.F. Yang, G. Zeng, RSC Adv. 6 (2016) 69.
[19] W. Wang, H. Cheng, B. Huang, X. Liu, X. Qin, X. Zhang, Y. Dai, J. Colloid Interface Sci. 442 (2015) 97.
[20] W.W. Dai, Z.Y. Zhao, Phys. Chem. Chem. Phys. 19 (2017) 9900.
[21] S. Yu, H. Huang, F. Dong, M. Li, N. Tian, T. Zhang, Y. Zhang, ACS Appl. Mater. Interfaces 7 (2015) 27925–27933.
[22] T. Xiong, H. Zhang, Y. Zhang, F. Dong, Chin. J. Catal. 36 (2015) 2155–2163.
[23] F. Chen, H. Huang, C. Zeng, X. Du, Y. Zhang, ACS Sustain. Chem. Eng. 5 (2017) 7777–7791.
[24] J. Feng, H. Huang, S. Yu, F. Dong, Y. Zhang, Phys. Chem. Chem. Phys. (PCCP) 18 (2016) 7851.
[25] Y. Sun, T. Xiong, F. Dong, H. Huang, W. Cen, Chem. Commun. 52 (2016) 8243.
[26] H. Huang, H. Ou, J. Feng, X. Du, Y. Zhang, Colloids Surf. A 518 (2017) 158–165.
[27] H. Huang, K. Xiao, N. Tian, Y. Guo, Y. Zhang, RSC Adv. 5 (2015) 81078–81086.
[28] C. Wang, Y. Ao, P. Wang, J. Hou, J. Qian, S. Zhang, J. Hazard. Mater. 178 (2010) 517.
[29] Z.M. El-Bahy, A.A. Ismail, R.M. Mohamed, J. Hazard. Mater. 166 (2009) 138–143.
[30] Y. Ao, J. Xu, S. Zhang, D. Fu, Appl. Surf. Sci. 256 (2010) 2754–2758.
[31] J.H. Park, S. Kim, A.J. Bard, Nano Lett. 6 (2006) 24–28.
[32] T. Xiong, F. Dong, Y. Zhou, M. Fu, W.K. Ho, J. Colloid Interface Sci. 447 (2015) 16.
[33] F. Vasiliu, L. Diamandescu, D. Macovei, C.M. Teodorescu, D. Tarabasanu-Mihaila, A.M. Vlaicu, V. Parvulescu, Top. Catal. 52 (2009) 544–556.
[34] J. Xu, Y. Ao, D. Fu, Appl. Surf. Sci. 256 (2009) 884–888.
[35] X.Z. Shen, Z.C. Liu, S.M. Xie, J. Guo, J. Hazard. Mater. 162 (2009) 1193–1198.
[36] S.H. Park, D. Ahn, Appl. Phys. Lett. 94 (2009) 083507.
[37] H. Li, T. Hu, J. Liu, S. Song, D. Na, R. Zhang, W. Hou, Appl. Catal. B: Environ. 182 (2016) 431–438.
[38] H. Huang, K. Xiao, Y. He, T. Zhang, F. Dong, X. Du, Y. Zhang, Appl. Catal. B: Environ. 199 (2016) 75–86.
[39] J. Han, J. Meeprasert, P. Maitarad, S. Nammuangruk, L. Shi, D. Zhang, J. Phys. Chem. C 120 (2016) 1523–1533.
[40] G. Li, Z. Lian, W. Wang, D. Zhang, H. Li, Nano Energy 19 (2016) 446–454.
[41] G. Li, B. Jiang, S. Xiao, Z. Lian, D. Zhang, J.C. Yu, H. Li, Environ. Sci. Process. Impacts 16 (2014) 1975–1980.
[42] S. Chen, T. Takata, K. Domen, Nat. Rev. Mater. 2 (2017) 50.
[43] Z. Zou, J. Ye, K. Sayama, H. Amp, Arakawa, Nature 414 (2001) 625.
[44] X.M. Qi, M.L. Gu, X.Y. Zhu, J. Wu, H.M. Long, K. He, Q. Wu, Chem. Eng. J. 285 (2016) 11–19.
[45] J. Wu, C. Li, X. Zhao, Q. Wu, X. Qi, X. Chen, T. Hu, Y. Cao, Appl. Catal. B: Environ. 176–177 (2015) 559–569.
[46] X. Zhou, J. Wu, J. Zhang, P. He, J.X. Ren, J.J. Zhang, J. Lu, P.K. Liang, K. Xu, F. Shui, Mater. Lett. 205 (2017) 173–177.
[47] P. Patiphatpanya, A. Phuruangrat, S. Thongtem, T. Thongtem, Mater. Lett. 209 (2017) 264–267.
[48] R. Zhou, J. Wu, J. Zhang, H. Tian, P. Liang, T. Zeng, P. Lu, J. Ren, T. Huang, X. Zhou, Appl. Catal. B: Environ. 204 (2017) 465–474.
[49] X.C. Song, Y.L. Qi, Y.F. Zheng, Mutat. Res. 12 (2016) 03.
[50] W. Wang, B. Huang, X. Ma, Z. Wang, X. Qin, X. Zhang, Y. Dai, M.H. Whangbo, Chemistry (Weinheim an der Bergstrasse, Germany) 19 (2013) 14777.
[51] X. Zhou, J. Wu, Q. Li, T. Zeng, Z. Ji, P. He, W. Pan, X. Qi, C. Wang, P. Liang, J. Catal. 355 (2017) 26–39.
[52] S.D. Nguyen, J. Yeon, S.H. Kim, P.S. Halasyamani, J. Am. Chem. Soc. 42 (2011) 12422–12425.
[53] L. Zhang, C.G. Niu, G.X. Xie, X.J. Wen, X.G. Zhang, G. Zeng, ACS Sustain. Chem. Eng. 5 (2017) 4619–4629.
[54] S. Liang, Y. Wang, S. Cinnirella, N. Pirrone, Environ. Sci. Technol. 49 (2015) 3566.
[55] S. Hu, F. Zhou, L. Wang, J. Zhang, Catal. Commun. 12 (2011) 794–797.
[56] W.U. Jiang, L.I. Chaoen, X. Chen, J. Zhang, L. Zhao, T. Huang, T. Hu, C. Zhang, B. Ni, X. Zhou, J. Ind. Eng. Chem. 46 (2016) 416–425.
[57] W.U. Jiang, C. Li, G. Li, F.H. Tian, K.S. Schanze, H. Li, ACS Appl. Mater. Interfaces 9 (2017) 16960–16967.
[58] Z. Zhang, J.T. Yates Jr, Chem. Rev. 112 (2012) 5520.
[59] L. Zhao, C. Li, Y. Wang, H. Wu, L. Gao, J. Zhang, G. Zeng, Appl. Catal. B: Environ. 198 (2016) 420–430.